The Shortening of MWNT-SPION Hybrids by Steam Treatment Improves Their Magnetic Resonance Imaging Properties In Vitro and In Vivo

Laura Cabana, Maxime Bourgognon, Julie T.-W. Wang, Andrea Protti, Rebecca Klippstein, Rafael T. M. de Rosales, Ajay M. Shah, Josep Fontcuberta, Ester Tobías-Rossell, Jane K. Sosabowski, Khuloud T. Al-Jamal, and Gerard Tobias**

Carbon nanotubes (CNTs) have been advocated as promising nanocarriers in the biomedical field. Their high surface area and needle-like shape make these systems especially attractive for diagnostic and therapeutic applications. Biocompatibility, cell internalization, biodistribution, and pharmacokinetic profile have all been reported to be length dependent. In this study, further insights are gotten on the role that the length of CNTs plays when developing novel contrast agents for magnetic resonance imaging (MRI). Two samples of CNTs with different length distribution have been decorated with radio-labeled iron oxide nanoparticles. Despite characterization of the prepared hybrids reveals a similar degree of loading and size of the nanoparticles for both samples, the use of short CNTs is found to enhance the MRI properties of the developed contrast agents both in vitro and in vivo compared to their long counterparts.

1. Introduction

Carbon nanotubes (CNTs) are being widely investigated for a diverse array of biomedical applications.[1] Their high surface area, nanoscopic dimensions with a hollow core, excellent mechanical properties, and good electrical conductivity make them appealing for diversified biological purposes. These include tissue scaffolds, bone prosthetics, neural interfaces, cellular growth, stem cell differentiation, biosensors, drug delivery, and biomedical imaging.[1,2] Both drug delivery and

Dr. L. Cabana, Prof. J. Fontcuberta, Dr. G. Tobias
Institut de Ciència de Materials de Barcelona (ICMAB-CSIC)
Campus UAB
08193 Bellaterra, Barcelona, Spain
E-mail: gerard.tobias@icmab.es

M. Bourgognon, Dr. J. T.-W. Wang, Dr. R. Klippstein, Dr. K. T. Al-Jamal
Institute of Pharmaceutical Science
King's College London
London SE1 9NH, UK
E-mail: khuloud.al-jamal@kcl.ac.uk

Dr. A. Protti, Dr. R. T. M. de Rosales
Division of Imaging Sciences and Biomedical Engineering
King's College London
St. Thomas' Hospital
London SE1 7EH, UK

Dr. A. Protti, Prof. A. M. Shah
Cardiovascular Division
James Black Centre
British Heart Foundation Centre of Excellence
King's College London
London SE5 9NU, UK

E. Tobías-Rossell
Escola Universitària de Ciències de la Salut
de Manresa
Universitat de Vic-Universitat Central de Catalunya
Av. Universitària 4-6, 08242, Manresa, Barcelona, Spain

Dr. J. K. Sosabowski
Centre for Molecular Oncology
Barts Cancer Institute
Queen Mary University of London
London EC1A 7BE, UK

DOI: 10.1002/smll.201502721

imaging take advantage of the needle-like shape of the CNTs which confers these materials with superior flow dynamics and an enhanced capacity to penetrate cellular membranes compared to spherical nanoparticles. CNTs are flexible structures and as such can bend and allow the interaction with cells through multiple binding sites.[2]

As a consequence of its use for biomedical applications, concerns have been raised on their potential cytotoxicity. As-produced CNTs contain several impurities, namely, amorphous, graphitic nanoparticles, and metal particles (from the catalysts employed in the CNT's growth). Early pharmacological studies reported on the cytotoxicity of as-prepared CNTs, but it was later shown that the observed toxicity was likely due to the presence of metal nanoparticles[3] or from long nanotubes (>15 μm).[4] The effect of as-prepared CNTs on human epidermal keratinocytes cells was investigated back in 2003,[5] showing the production of free radicals and reactive oxygen species in relation to the presence of residual metal catalysts.[3] These impurities are not the sole source of potential cytotoxicity, since long CNTs were found to induce acute and chronic peritoneal inflammation in mice.[4] It is also suggested that CNT nanosystems could induce inflammatory responses if the length is larger than the size of phagocytic cells.[6] It has also been reported that long fibers cannot be completely engulfed by macrophages leading to the incomplete internalization of the CNTs, which consequently could interfere with the plasma membrane function.[7] Nevertheless, it is still a general consensus within the scientific community that CNTs hold great potential in biomedical applications provided they have been properly purified, shortened, and dispersed either via covalent or noncovalent strategies, thus rendering a biocompatible nanoplatform.[8]

The length of the CNTs has been shown to have a major impact on key pharmacological aspects including cell internalization, in vivo biodistribution, and pharmacokinetic profiles. By exposing cells to multiwalled CNTs (MWNTs) of different lengths, it was shown by Bussy et al. that the percentage of cells containing MWNTs was significantly higher for short CNTs, indicating they were more easily internalized by the cells.[6] Moreover, it has also been reported that short CNTs were accumulated in the tissues to a lesser extent and could undergo faster renal excretion compared to their long counterparts.[9]

Several strategies have been developed to purify and shorten CNTs to efficiently obtain biocompatible CNTs including treatments with oxidizing acids,[10] fluorination,[11] and steam.[12] Steam has been proposed as a method to remove the impurities present during the CNT growth while reducing the impact on the wall structure of the CNTs. In contrast to oxygen that above a given temperature reacts with CNTs in a fast manner, steam being a milder oxidizing agent allows a better control of the purification process.[12,13] In addition, the length of the nanotubes can be easily modulated by a mere change in the steam exposure time, with reactions that can last for several hours at temperatures around 900 °C.[13]

A common approach towards the development of CNT-based diagnostic agents for biomedical imaging is via the formation of hybrid nanostructures.[14] One can take advantage of the hollow cavity of CNTs, susceptible of being filled with a wide variety of materials,[15] to encapsulate a chosen imaging agent.[16] In this way the external walls remain available for the attachment of dispersing and targeting moieties. The second strategy consists of the external decoration with either inorganic nanoparticles or molecular tags.[17] CNT-based imaging agents have been developed aiming to improve the sensitivity and contrast of clinically relevant modalities including nuclear imaging (single photon emission computed tomography (SPECT), positron emission tomography (PET), and magnetic resonance imaging (MRI)). Nuclear imaging records the radiation emitted from the radiopharmaceutical within the body (inside-out) rather than the radiation generated by external sources crossing the body (e.g., X-rays). Several radiolabeled-CNTs have been developed by chelation of chosen radionuclides to the external CNT walls for both diagnosis and therapeutic purposes.[17b,c,18] On the other hand, MRI does not involve ionizing radiation and is experiencing a sustained increase in demand with over 25 000 scanners in use worldwide.[19] Inherent MRI contrast is a function of proton density, relaxation times, and magnetic susceptibility. Since it is rather difficult to alter the water content of tissues, many diagnostic questions require the use of external contrast agents. Contrast agents based on gadolinium and iron have been the main focus of attention. Positive contrast agents based on gadolinium-loaded CNTs have shown promising results up to the preclinical level.[16d,20] Several studies have reported the preparation and use of superparamagnetic iron oxide nanoparticles (SPION) attached to CNTs for biomedical imaging applications.[17a] These behave as negative contrast agents, increasing the R_2 and R_2^* relaxation rates. Choi et al. prepared Fe catalyst-grown SWNT (length not reported) and confirmed the formation of paramagnetic iron oxide at the tip of CNTs. Phagocytic cells incubated with Fe catalyst-grown SWNTs were then imaged by MRI and near-infrared fluorescence.[21] Yin et al. conjugated SPION (7–8 nm in diameter) to MWNTs (100–300 nm length) and actively targeted the hybrids to cancer cells using folic acid.[22] After incubation with cells over-expressing folate receptor (HeLa cells), the targeted magnetic hybrid increased the in vitro R_2 relaxation rate of incubated cells. Wu et al. loaded Fe_3O_4 nanoparticles (average size of 4.5 nm) to the surface of MWNTs (0.5–2 μm length) and showed an MR signal enhancement in the liver and spleen after intravenous injection of the hybrid, highlighting the accumulation of such hybrid into the reticular endothelial system (RES).[23] Recently, Liu et al. conjugated SPION (diameter of 9 nm) to MWNTs (length not reported) by electrostatic interaction, which were injected intravenously into mice bearing liver metastases.[24] Increases in liver tumor contrast ratio between tumor and healthy tissue region facilitated the diagnosis of liver metastases. To further expand the capabilities of CNTs contrast agents, we have recently shown that CNTs can serve as a nanoplatform to combine both imaging modalities (SPECT/CT and MRI) thus affording dual imaging. This was achieved by radiolabeling SPION-decorated MWNTs with ^{99m}Tc.[25] In the present report, we take advantage of this newly introduced concept to get further insights on the role that the CNTs' length has on the development of novel contrast agents. The use of steam shortened

MWNTs not only allows the modulation of the pharmacological profile of the resulting contrast agents but is also found to enhance the R_2^* magnetic properties both in vitro and in vivo compared to their long counterparts.

2. Results and Discussion

2.1. Synthesis of Different Length of Iron Oxide-MWNTs Hybrids

As-received MWNTs were treated by steam to remove carbonaceous impurities that are present as secondary products during the CNTs' growth, namely, amorphous carbon and graphitic particles. The graphitic particles can in turn cover catalytic particles and inhibit their dissolution by an acid wash. After the steam treatment the metal particles become exposed and can be easily removed by HCl.[26] The length of the MWNTs can be modulated by changing the time of the steam treatment.[13] For the preparation of long MWNTs (L-MWNT) the sample was exposed to steam for 1.5 h, whereas for short MWNTs (S-MWNT), steam treatment of 15 h was employed. Afterward, oxygen bearing functionalities were added onto the CNTs by treating with nitric acid.[10] In this respect, the removal of amorphous carbon is necessary to allow a proper functionalization of the CNTs' walls.[27] As described in the Introduction, the use of oxidizing acids can also shorten the nanotubes.[10] Next, the synthesis of the iron oxide nanoparticles was conducted in situ following a previously reported protocol.[25] The presence of oxygen bearing functionalities on the backbone structure of the MWNTs facilitates the coating since these moieties act as anchoring groups during the formation of the nanoparticles. The iron oxide nanoparticles were prepared in situ by decomposition of iron acetate, which was employed as an iron precursor.

2.2. Physicochemical Characterization of L-SPION-MWNT and S-SPION-MWNT

The length distribution of both samples, after the steam and nitric acid treatments, was determined by measuring individual nanotubes from low resolution transmission electron microscopy (TEM) images (**Figure 1**A,B and Figure S1, Supporting Information). The insets in Figure 1A,B show the resulting histograms (group sizes of 150 nanotubes) and the box plot analysis is presented in Figure S2 and Table S1 (Supporting Information). The median lengths for the long (L-MWNT) and short nanotubes (S-MWNT) are 0.85 and 0.30 μm, respectively. Actually the decrease in length becomes apparent by visual inspection of the TEM images (Figure 1A,B). Figure 1C,D presents TEM images of both the L-MWNT and S-MWNT after being decorated with the nanoparticles (L-SPION-MWNT and S-SPION-MWNT, respectively). It is interesting to note that the short nanotubes appear to present a larger amount of π–π interactions leading to the formation of small bundles; for additional TEM images see Figure S3 (Supporting Information) (L-SPION-MWNT) and Figure S4 (Supporting Information) (S-SPION-MWNT). The amorphous "coating" that is seen in some of the images is due to the Pluronic F-127 employed for the dispersion of the nanotubes. Pluronic block co-polymers are being widely employed to improve the water-solubility and reduce aggregation of nanocarriers.[28] It was employed in this study to improve the water-dispersibility and reduce aggregation of MWNT hybrids. The use of biocompatible block copolymers is getting an increased attention to render colloidally stabilized CNTs.[16e] The prepared long and short hybrids present a good and stable aqueous dispersibility in 1% Pluronic F127 (the study was performed up to 24 h; Figure S5, Supporting Information). The amount of nanoparticles present in the resulting hybrids was quantitatively determined by thermogravimetric analysis (TGA) (Figure S6, Supporting Information). The samples were heated under flowing air until their complete combustion. Therefore, considering the nanoparticles as Fe_2O_3, the residue obtained after the TGA

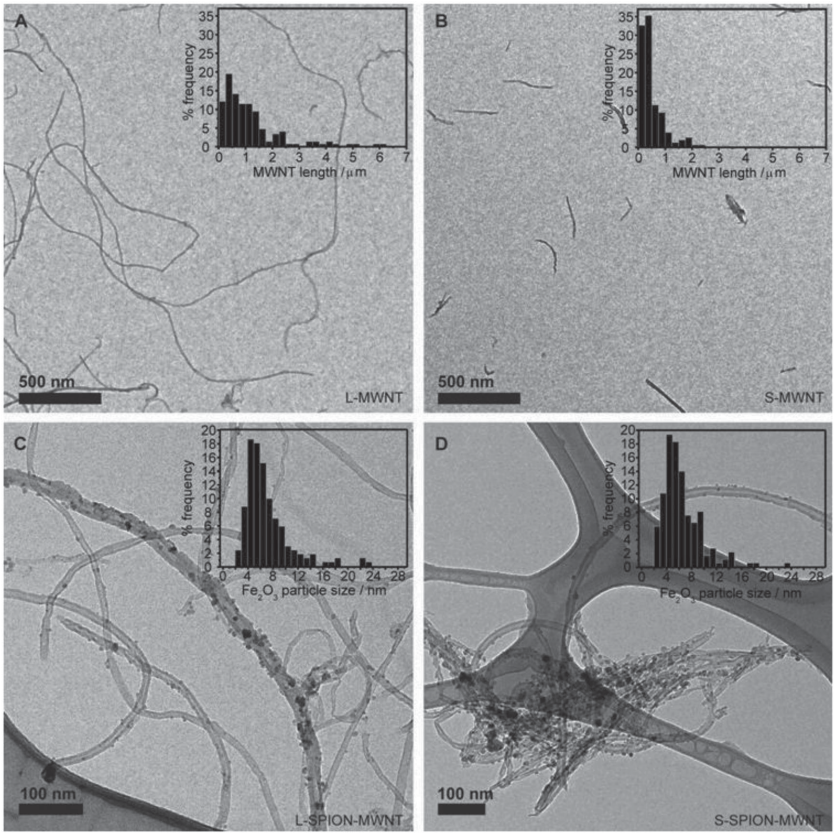

Figure 1. Transmission electron microscopy (TEM) analysis of the prepared hybrids. A,B) TEM images and length distribution histograms of (A) L-MWNT and (B) S-MWNT. C,D) TEM images and SPION particle size distribution histograms (insets) of (C) L-SPION-MWNT and (D) S-SPION-MWNT.

analysis corresponds to the iron oxide present in each sample. In the case of L-SPION-MWNT, the residue is of 33.5 wt% and was of 29.5 wt% for S-SPION-MWNT. Since both hybrids display a similar degree of SPION loading, the amount of SPION presented for a given mass (or length) of nanotube will be the same. Therefore, each individual long nanotube will at the end possess a larger amount of nanoparticles per nanotube than a single short nanotube.

The size, shape, and distribution of the nanoparticles were examined by TEM (Figure 1C,D). The nanoparticles appear to be well spread along the MWNT walls. The diameter of about 180 nanoparticles was evaluated for both the L-SPION-MWNT and the S- SPION-MWNT and the resulting histograms are displayed as an inset in the figures. Since the studied groups of nanoparticles present a nonsymmetric particle size distribution it is not correct to determine an average mean size so a box plot analysis was performed (**Figure 2** and Table S1, Supporting Information). Box plot analysis reveals a similar particle size distribution of the nanoparticles regardless of the length of the MWNTs, with almost no particles being bigger than 13.1 nm (maximum adjacent observation for both the S- SPION-MWNT and the L- SPION-MWNT). The median particle size is about 5.9 nm (5.7 nm in the S- SPION-MWCNTs and 6.1 nm in the L- SPION-MWNT). We employed nonparametric tests to assess whether the median and the particle size distribution of the two groups of nanoparticles had significant differences or not. The median test was used for the former, and both the U test of Mann–Whitney and the Kolmogorov–Smirnov test are employed for the latter. The statistical hypothesis testing showed no significant differences (p-value > 0.05). The

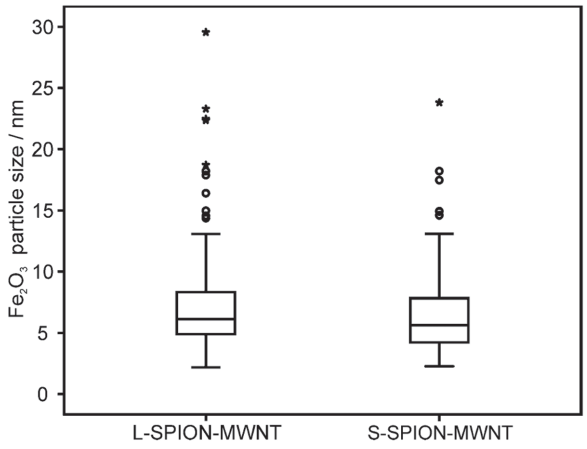

Figure 2. Box plot analysis of the particle size distribution in S-SPION-MWNT and L-SPION-MWNT. Empty circles indicate outliers and asterisks far outliers.

structure of the prepared nanoparticles was further investigated by X-ray diffraction (XRD) and X-ray photoelectron spectroscopy (XPS) (**Figure 3**). The two hybrids present the same XRD diffraction patterns with peaks arising from the carbon nanotubes (PDF—powder diffraction file—750444) and from the presence of iron oxide nanoparticles which are in agreement with both maghemite (γ-Fe_2O_3; PDF 391346) and magnetite (Fe_3O_4; PDF 740748). The small particle size of the nanoparticles is also reflected by the broad peaks present in the diffraction pattern. The presence of maghemite and magnetite can be discerned by XPS analysis over the Fe 2p region.[29] The "shake-up" satellite structure at 720 eV

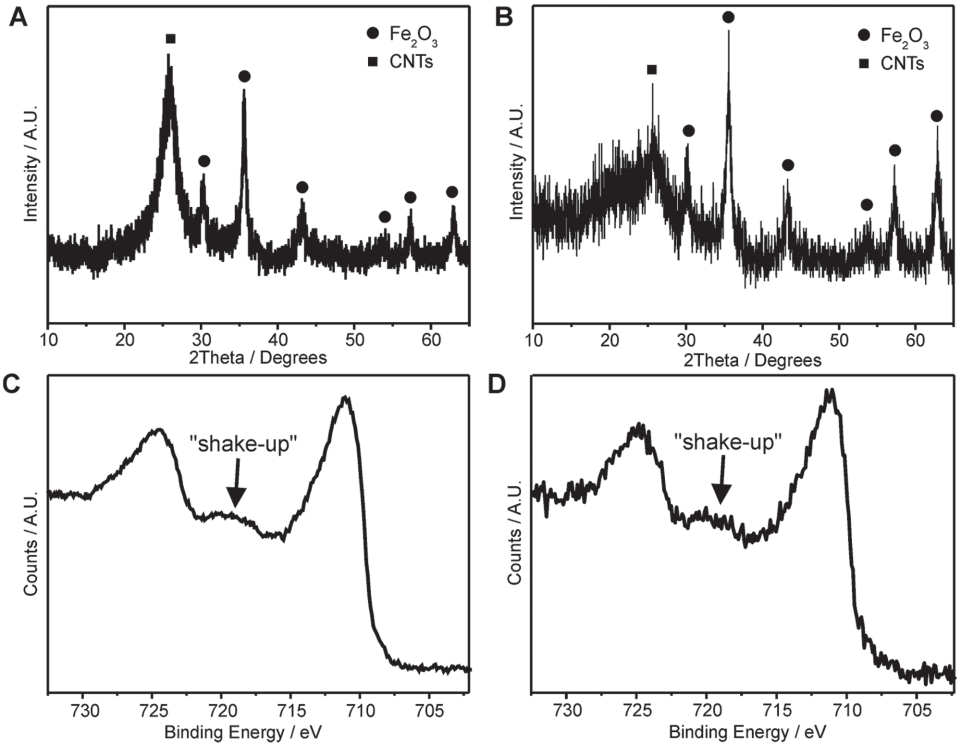

Figure 3. X-ray diffraction (XRD) pattern (top) and X-ray photoelectron spectroscopy (XPS) (bottom) of the Fe 2p region. A,C) L-SPION-MWNT and B,D) S-SPION-MWNT.

observed in both the short and long hybrids is distinctive of maghemite (γ-Fe_2O_3).

2.3. Phantom MR Imaging and *R*2* Relaxation Measurements

To compare the MR imaging properties of hybrids, samples with concentrations ranging from 0.125 to 1.25 × 10^{-3} M (Fe) were prepared and imaged in a preclinical scanner at 7 Tesla. L-SPION-MWNT, S-SPION-MWNT, and Endorem were dispersed by sonication before being resuspended in 1% agar solution (phantoms). Relaxation times (R_2*) of L-SPION-MWNT, S-SPION-MWNT, and Endorem calculated from their signal decay were plotted against Fe concentration (**Figure 4**).

R_2* measurements are significantly higher than R_2 at high field, but their relaxivity pattern should be comparable. Even though R_2 is a more clinically relevant parameter, R_2* is preferred to explore relaxation properties of iron oxide contrast agent at high field as it increases the measurement sensitivity. Good linear regressions ($R^2 > 0.98$) were obtained and their slopes, defined as relaxivity values (r_2*), indicated that S-SPION-MWNT exhibits higher r_2* value (530 s^{-1} mM^{-1}) compared to L-SPION-MWNT (417 s^{-1} mM^{-1}). Both hybrids displayed higher r_2* values compared to Endorem (308 s^{-1} mM^{-1}). To investigate if the enhanced r_2* value of S-SPION-MWNT resulted from the magnetic properties of pristine MWNT, relaxivity measurements of S-MWNT and L-MWNT (without SPION decoration) were carried out (Figure S7, Supporting Information). R_2 relaxivity measurements of L-MWNT and S-MWNT were very low (<1 s^{-1} mM^{-1}) and not different for both hybrids.

2.4. Magnetic Properties of L-SPION-MWNT and S-SPION-MWNT

The higher r_2* values observed for the S-SPION-MWNT compared to the L-SPION-MWNT cannot be explained from the physicochemical characterization performed so far since both samples contain particles of Fe_2O_3 with similar sizes, as assessed by box plot analysis. Wilson and co-workers reported that ultrashort SWNTs (60–80 nm in length) have an intrinsic and significant contribution to the MRI signal.[30] In our case a negligible MRI signal was observed in both of the steam treated samples (L-MWNT and S-MWNT) in the absence of SPION (Figure S7, Supporting Information). Therefore, we next performed magnetic measurements of both hybrids, trying to discern the origin of the enhanced relaxivity when short nanotubes are employed.

First, hysteresis loops performed at 300 K are shown in **Figure 5**A,B. It is clear that samples have a very similar saturation magnetization and no remnant magnetization is observed at room temperature after removal of the external magnetic field confirming that magnetic particles are similar in the S-SPION-MWNT and the L-SPION-MWNT samples and have a superparamagnetic behavior at this temperature. Figure 5C,D presents the zero-field cooling (ZFC) and field cooling (FC) curves of both hybrids. These experiments were done as it is known that differences on particles size distribution and dipolar magnetic interactions among particles translate into differences in ZFC-FC curves. The ZFC curve is measured upon warming using a field of 100 Oe, after cooling down the sample in nominally zero magnetic field; in the FC study there is an applied field of 100 Oe. The observed divergence of the ZFC and FC data upon cooling is the common behavior of a system of superparamagnetic particles. A gradual increase of magnetization is observed in FC data when decreasing the temperature, reflecting the reduction of the thermally induced magnetic disorder and the progressive field-induced orientation of the magnetic moment of each particle. In contrast, in the ZFC curves the magnetization decreases when decreasing the temperature. In the ZFC measurement, when cooling to a particular temperature, the thermal energy becomes smaller than the magnetic anisotropy energy and therefore the magnetic moment of the nanoparticle gets blocked in a direction dictated by its magnetic anisotropy axis. For a collection of noninteracting SPIONs, that is SPIONs are far apart from each other in the absence of any magnetic field (ZFC), this direction is randomly distributed and thus the overall magnetization should vanish at the lowest temperature. This is a way the magnetization is small at low temperature in a ZFC process. When warming and measuring under a given magnetic field, the sample magnetization gradually increases and thus the ZFC displays a maximum (so-called blocking temperature T_B) and merges the FC curve. For a system on noninteracting SPIONs, T_B is determined exclusively by the magnetic anisotropy energy ($E_a = K_aV$) where K_a is the anisotropy constant of the nanoparticle and V its volume. In the present case, the composition of SPIONs is seen to be identical in both samples (as inferred for the structural and spectroscopic data in Figure 3, and the saturation magnetization of Figure 5AB). Their shape, size,

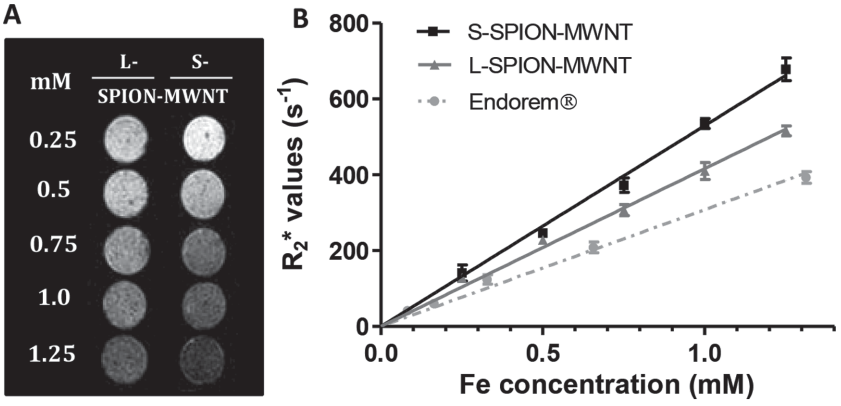

Figure 4. Phantom MR imaging of hybrids and Endorem. Samples were dispersed in 1% agar solution and imaged using a 7 Tesla (7T) preclinical MR scanner. A) Phantom MR imaging of Endorem, S-SPION-MWNT, and L-SPION-MWNT; B) R_2* relaxation rate analysis as a function of Fe concentration. Results are presented as mean ± SD showing higher r_2* relaxivity for S-SPION-MWNT ($n = 3$).

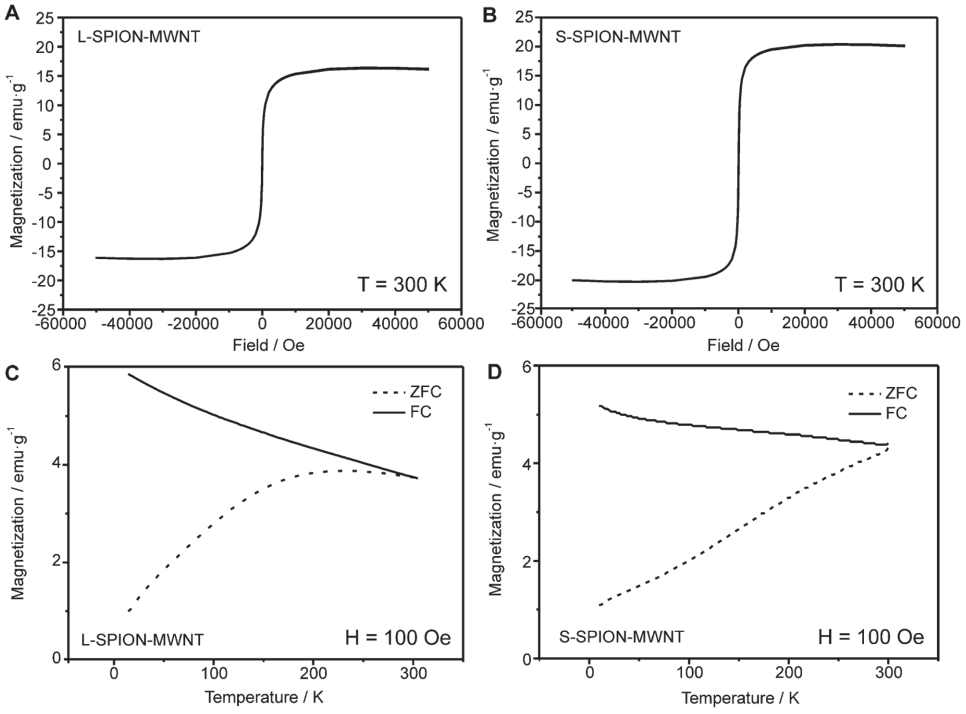

Figure 5. Hysteresis loops at 300 K after subtracting the linear background (top) and zero field-cooling and field-cooling curves (100 Oe), recorded using a field of 100 Oe (bottom). A,C) L-SPION-MWNT and B,D) S-SPION-MWNT.

and size-distributions are also virtually identical. Therefore, E_a should be similar in both samples and correspondingly T_B values are expected to be the same. This however was not the case, and as can be seen in Figure 5C,D, L-SPION-MWNT and S-SPION-MWNT display different ZFC-FC response curves. In L-SPION-MWNT, T_B is visible at ≈175 K and ZFC-FC curves merge at $T_B \approx 290$ K. Overall, the ZFC-FC curves of S-SPION-MWNT show a similar shape, although a slightly higher merging ZFC-FC temperature was observed. The merging of the ZFC-FC curves at high temperatures has been previously described for nanoparticles presenting broad size distribution.[31] However, as stated above, the nanoparticles in both L-SPION-MWNT and S-SPION-MWNT present a narrow and statistically similar size distribution. The presence of outliers/far-outliers (11 nm L-SPION-MWNT and 7 nm in S-SPION-MWNT; Figure 2) is also found to have no effect on the magnetic response of the material (Figure 5A,B). Differences in T_B should thus be related to differences in magnetic interactions between SPIONs; indeed nanoparticle interaction has an important influence in boosting stability of arrangement of magnetic nanoparticles.[31] This interaction may be reflected in the MR properties. The distance between SPIONs on an individual MWNT should be similar as the number of SPIONs per unit MWNT's length was similar for both samples. The interparticle interactions, among SPIONs, might arise from SPIONs sitting on different nanotubes. As described under TEM analysis results, S-SPION-MWNT tends to form small bundles, which suggests an enhanced interparticle interaction to occur compared to L-SPION-MWNT. It is hypothesized that these interactions make them behave as one cluster, producing an increase in the blocking temperature.[32] Indeed, the hysteresis loops recorded at low temperature (Figure S8, Supporting Information) clearly show a minor but visible coercivity that reflects the interparticle interaction. Phantom MR imaging of the hybrids significantly revealed a higher relaxivity values for S-SPION-MWNT. This could be explained by the higher interaction between the SPION when MWNTs have shorter length in agreement with the magnetic measurements. As a result of this interaction, the cluster itself might be considered as a large magnetized sphere. The total magnetization is aligned to the magnetic field and due to the large size the secular term of the relaxation rate is affected

$$R_2 = \frac{1}{T_2} = \frac{16 f_a \Delta\omega^2 \tau_D}{45} \quad (1)$$

The secular contribution derives from the outsphere diffusion theory.[33] This refers to $\Delta\omega\tau_D < 1$, where $\Delta\omega$ is the difference between the frequencies of the local field experienced by a proton in the cluster surface and the one experienced by a proton in the bulk, and τ_D is the diffusion time around the cluster, which increases with cluster size.[34] In Equation (1), f_a is the volume fraction occupied by the cluster. This secular contribution significantly describes an increase in R_2 values at high fields.[35] Consequently, for S-SPION-MWNT the values were higher than for L-SPION-MWNT, which have a more diffused cluster. A similar phenomenon has been reported for gadofullerenes (gadolinium endohedralmetallofullerenes) which have been also investigated as paramagnetic MRI contrast agents. Gadofullerenes tend to form aggregates, small clusters, which is at the origin of much of their relaxivity enhancement.[36] As a result, when the gadofullerenes are disaggregated (individualized), the substantial enhancement over the clinically available contrast agents is mostly lost.

2.5. In Vitro Cytotoxicity, MR Imaging, and Uptake Ability of Hybrids by ICP-MS in J774A.1 Cells

In vitro cytotoxicity of the hybrids was assessed using the mouse macrophage cell line J774 (see Supporting Information Figures S9 and S10). We observed minimal effects of both types of hybrids on cell proliferation and lack of apoptosis at relatively high concentrations up to 72 h of incubation. The ability of SPION-MWNT hybrids to be internalized within cells and conserve their imaging properties in vitro was then studied. L-SPION-MWNT, S-SPION-MWNT, and Endorem were incubated with J774A.1 cells at 12 and 24 μg (Fe) per mL for 24 h. Perls' staining demonstrated the co-localization of CNTs and Fe within J774A.1 cells (**Figure 6**A).

To measure the MR imaging properties of internalized hybrids, J774A.1 cells were detached, fixed, and resuspended in 0.5% agarose solution at a final density of 1×10^6 cells per 200 μL and imaged at 7 Tesla. Figure 6B,C represents the in vitro phantom imaging and the relaxation rates measured from their signal decays. J774A.1 cells incubated with both hybrids showed higher R_2* relaxation rate compared to cells exposed to Endorem. J774A.1 treated with S-SPION-MWNT displayed higher relaxation rate (R_2*) than cells exposed to L-SPION-MWNT and Endorem (at 24 μg mL^{-1}). These results confirmed that the shortening of SPION-MWNT increased the in vitro negative contrast imaging properties of hybrids. The intracellular Fe content (per 1×10^5 cells) was then measured by inductively coupled plasma mass spectrometry (ICP-MS) to assess if MR enhancement effect was due to higher uptake capacity of S-SPION-MWNT into cells or due to their intrinsically enhanced MR properties. J774A.1 cells treated with S-SPION-MWNT and L-SPION-MWNT showed higher iron uptake than cells incubated with Endorem (**55D**). However, no significant difference in intracellular Fe content was observed between the two types of the hybrids, suggesting that the enhanced MR signals of S-SPION-MWNT were due to intrinsic enhancement agreeing with phantom studies. According to the performed magnetic measurements, this intrinsic enhancement of the MR signals when using short MWNT could arise from the tendency that short MWNT forms small bundles, thus increasing the interactions between SPION from neighboring S-MWNT compared to L-MWNT. This is in good agreement with the work of Bardi et al. on the uptake of functionalized MWNTs (*f*-MWNTs) by neural tissue cells in vivo.[37] The authors observed that long MWNTs appeared either as small clusters enclosed within membranous intracellular vesicles or as individualized nanotubes residing in the cytoplasm. In contrast, short MWNTs were always observed in clusters, predominantly taken up by neuronal cells as clusters wrapped within intracellular vesicles and very rarely seen individualized in the cytoplasm.[37] The length of the short and long MWNTs employed by Bardi et al. was similar to the length distribution used in the present study (Bardi et al.: 0.2–0.3 μm and 0.5–1 μm for short and long MWNTs, respectively/present study: 0.3 μm and 0.85 μm median values for short and long MWNTs, respectively).

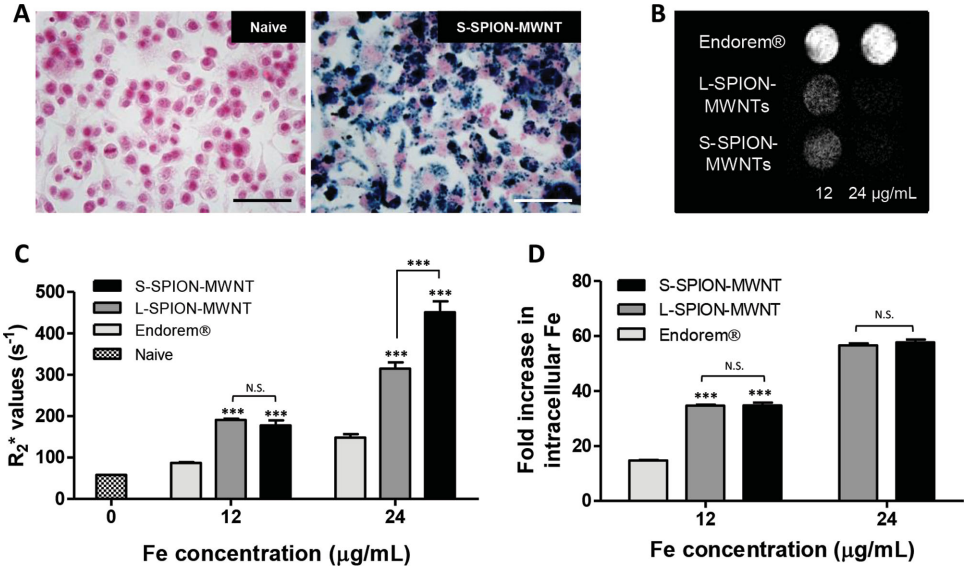

Figure 6. In vitro MR imaging of J774A.1 cells exposed to SPION-MWNT and Endorem. J774 cells were incubated with Endorem, L-SPION-MWNT, or S-SPION-MWNT at 12 or 24 μg mL^{-1} (Fe) for 24 h. A) Perl's staining of J774A.1 cells exposed to 24 μg mL^{-1} (Fe) of S-SPION-MWNT for 24 h; B) In vitro T_2*-weighted MR images of J774A.1 cells exposed to SPION-MWNT and Endorem. After treatment, cells were washed with PBS, resuspended in 0.5% agarose at a density of 1×10^6 cells per 200 μL. Resulting phantoms were imaged at 7 Tesla; C) In vitro R_2* relaxation rate measurements. J774A.1 cells incubated with SPION-MWNT displayed higher R_2* values compared to cells exposed to Endorem. Cells exposed to S-SPION-MWNT at 24 μg mL^{-1} displayed the highest R_2* value ($n = 3$); D) Intracellular iron measurement of J774A.1 cells treated with SPION-MWNT or Endorem. Phantoms were digested overnight in nitric acid (>65%) and their iron content was assessed using ICP-MS. J774A.1 cells incubated with SPION-MWNT displayed a two to threefold intracellular Fe concentration increase compared to cells incubated with Endorem but the differences between cells treated with short and long hybrids were not significant (N.S.) ($n = 3$). *$p < 0.05$, **$p < 0.01$, ***$p < 0.001$ are relative to Endorem treated samples at equal Fe concentration or are calculated from the comparison between samples using analysis of variance (ANOVA) with post hoc analysis by the Tukey test. The scale bar corresponds to 50 μm.

2.6. Relaxation Rate of S-SPION-MWNT in Mice

Magnetic properties of S-SPION-MWNT and Endorem were compared in liver tissue after intravenous injection at 1.4 or 2.9 mg (Fe) per kg in mice. R_2* values were measured in living animals at 30 min, 24 h, and 8 d postinjection. Relaxation rate measurements on the liver from mice injected with Endorem at 1.4 mg (Fe) per kg showed highest value ($326.9 \pm 12.4\ s^{-1}$) at earliest scan time (i.e., 30 min after injection) which progressively decreased to background at 8 d postinjection ($120.3 \pm 25.2\ s^{-1}$) (**Figure 7**).

Such results were indicative of the rapid and vast accumulation of Endorem in the RES within 30 min. Following intravenous injection of S-SPION-MWNT in mice, relaxation rates in liver tissue increased from $251.1 \pm 12.0\ s^{-1}$ (30 min) to $347.1 \pm 26.2\ s^{-1}$ (24 h) before decreasing to $180.1 \pm 10.6\ s^{-1}$ (8 d). S-SPION-MWNT displayed uptake in the lung with a percentage reaching the liver and spleen, as will be presented later. Interestingly, 24 h after injection, the relaxation rate of the liver injected with S-SPION-MWNT ($347.1 \pm 26.2\ s^{-1}$) was comparable to that of Endorem ($316.9 \pm 15.9\ s^{-1}$). Furthermore, the relaxation rate of the liver treated with S-SPION-MWNT was consistently higher than that of Endorem at 8 d ($^*p < 0.05$). When the injected dose of S-SPION-MWNT was increased from 1.4 to 2.9 mg (Fe) per kg, R_2* measurements on the liver reached $495.3 \pm 51.5\ s^{-1}$ at 24 h (Figure S11, Supporting Information). Both injected dose of S-SPION-MWNT showed an increase in R_2* measurements from 30 min to 24 h and significantly higher R_2* values at 8 d compared to Endorem. R_2* measurements in the spleen of mice injected with 2.9 mg (Fe) per kg displayed consistently higher relaxation time for Endorem compared to S-SPION-MWNT.

2.7. Biodistribution Study of ^{99m}Tc-BP-S-MWNT in Mice after Intravenous Injection

To assess the fraction of short hybrids contributing to MR signals within the liver and to confirm their ability to exert dual-imaging property, S-SPION-MWNT biodistribution was investigated using the method we previously reported for L-SPION-MWNT adopted from Rosales et al.[25,38] A functionalized bisphosphonate (BP) named dipicolylamine-alendronate (DPA-ale) was utilized as a linker between the radioisotope ^{99m}Tc and SPION. The ^{99m}Tc-BP complex was mixed with S-SPION-MWNT for 30 min at 37 °C to form ^{99m}Tc-BP-S-MWNT. The radio-labeled hybrid was then washed to remove unbound ^{99m}Tc-BP and its labeling stability in phosphate buffered saline (PBS) and serum was confirmed (Figure S12, Supporting Information). Whole body SPECT/CT imaging was carried out at 30 min, 4 h, and 24 h after intravenous injection of ^{99m}Tc-BP-S-MWNT (4 MBq, 10 mg kg^{-1} hybrid) or ^{99m}Tc-BP (10 MBq) alone in C57BL/6 mice (**Figure 8**A).

The affinity of bisphosphonates molecules (^{99m}Tc-BP) for bone mineral tissue led to the accumulation of free ^{99m}Tc-BP into bone tissue. The high signal within the bladder revealed the predominant urinary excretion of the free ^{99m}Tc-BP. This result agrees with our previously published data.[38] In comparison, ^{99m}Tc-BP-S-MWNT accumulated mostly into the lungs, followed by the liver and spleen after 30 min of injection. A small fraction of ^{99m}Tc-BP-S-MWNT was found in the bladder, indicating that a fraction of the hybrid was excreted via the urinary tract. Because of the rapid decay of ^{99m}Tc (half-life = 6 h), the "virtual" loss of radioactivity was compensated by adjusting the signal intensity of later time points. No significant differences in the liver or spleen distribution over time, i.e., 4 h versus 24 h, were observed.

To assess quantitatively the organ biodistribution profile of S-SPION-MWNT, postmortem γ-scintigraphy was conducted. Major mouse organs were excised at 1, 4, and 24 h time points. As observed with SPECT/CT results, the lung, liver, and spleen were the organs showing the highest accumulation with 317.2% ± 32.0%, 36.1% ± 3.4%, and 41.2% ± 14.8% ID g^{-1} (percentage injection dose per gram of tissue), respectively (Figure 8B). Despite significant accumulation of ^{99m}Tc-BP-S-MWNT into the lungs, the hybrid was progressively cleared from this organ. In contrast, no clearance of ^{99m}Tc-BP-S-MWNT was observed for the liver and spleen. Blood clearance profile showed that 3.5% ± 0.8% ID mL^{-1} of blood was measured 30 min after injection (Figure 8C). Only 3.3% ± 0.4% ID was excreted via the urine, whereas only 0.41% ± 0.5% ID was measured in feces. To summarize, ^{99m}Tc-BP-S-MWNT predominantly accumulated not only into the lungs but also into the liver and spleen. Relocation of the hybrid from the lungs into the liver and spleen was observed over the 30 min–24 h period. Histological examinations of the liver, lung, spleen, and kidney confirm the presence of the hybrids in mouse organs by Perl's staining and also lack of histological changes in organs postinjection (see Supporting Information Figures S13 and S14).

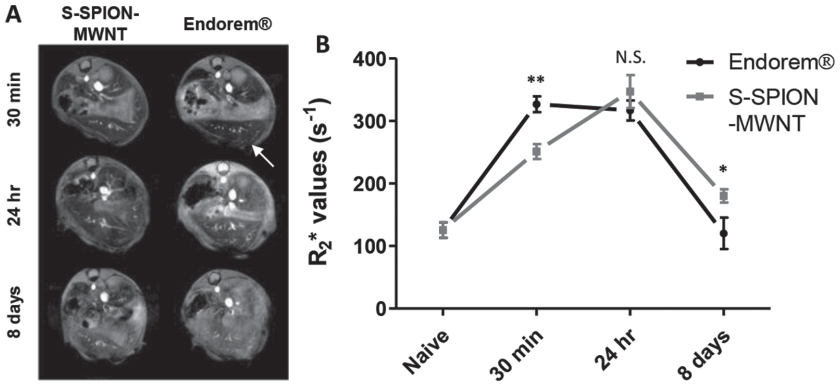

Figure 7. In vivo R_2*-weighted MR studies in the liver after intravenous injection of S-SPION-MWNT (1.4 mg (Fe) per kg). A) In vivo T_2*-weighted MR images at 7 T; B) In vivo R_2* relaxation rate measurements. R_2* relaxation rate analysis in the liver showed insignificantly different R_2* values between S-SPION-MWNT and Endorem, 24 h after injection ($n = 5$). $^*p < 0.05$, $^{**}p < 0.01$ relative to the naïve condition by analysis of variance (ANOVA) with post hoc analysis by the Tukey test.

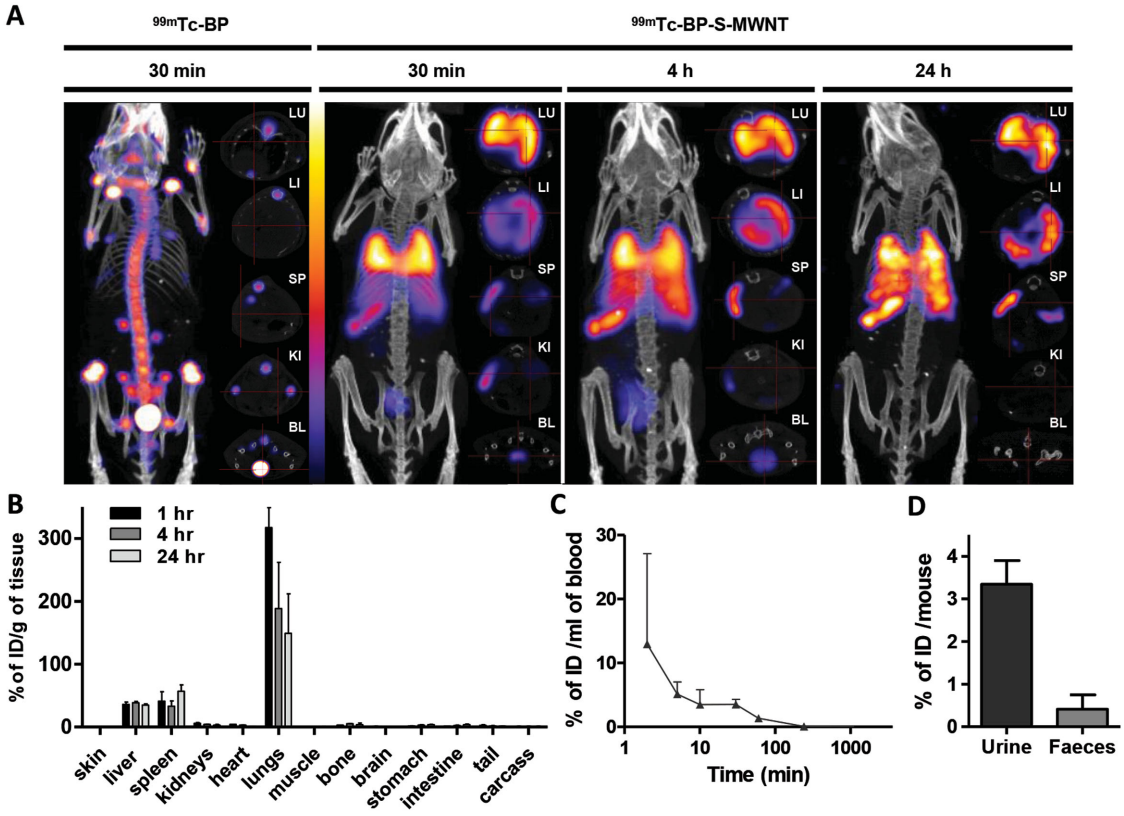

Figure 8. In vivo SPECT/CT images and organ biodistribution studies following intravenous injection of ^{99m}Tc-BP-S-MWNT. ^{99m}Tc-BP and S-MWNT-SPION were mixed for 30 min at 37 °C to form ^{99m}Tc-BP-S-MWNT. Unbound ^{99m}Tc-BP was removed following four centrifugation steps until limited amount of radioactivity (<1% of the total activity) was measured in the supernatant. Hybrids as 200 µg (4 MBq) or 100 µg (0.2 MBq) were injected intravenously for SPECT/CT imaging and γ-counting study, respectively. A) Whole body 3D SPECT/CT imaging; B) Organ biodistribution of ^{99m}Tc-BP-S-MWNT by γ-counting; C) Blood clearance profile. Blood samples from 2 min up to 24 h were collected after injection of ^{99m}Tc-BP-S-MWNT ($n = 3$); D) Excretion profile. Injected mice were kept in metabolic cages to collect urine and faeces. Cross sections in (A) were taken at the lung (LU), liver (LI), spleen (SP), kidney (KI), and bladder (BL). Results are expressed as mean ± SD ($n = 3$). Blue and yellow colors indicate low and high radioactivity signals, respectively.

3. Conclusions

The effect of CNT's length distribution on the development of novel contrast agents has been investigated. Hybrid materials based on CNTs with different lengths have been prepared via their decoration with radio-labeled SPION. Similar biodistribution of the shortened hybrid was observed in vivo by SPECT/CT imaging compared to the longer hybrid studied previously. Remarkably, both in vitro and in vivo studies revealed an enhancement in the MR signal when employing short CNTs in comparison with their long counterparts. Taking into account that a similar amount of intracellular Fe content was detected for both developed agents (long and short CNTs), the enhancement in the MR signal when employing short CNTs was therefore found to be intrinsic in agreement with phantom studies. Visual inspection of the prepared hybrids by transmission electron microscopy showed a larger degree of interparticle interactions in the sample of short CNTs, which is in agreement with Superconducting Quantum Interference Device (SQUID) magnetic measurements. These interparticle interactions could be at the origin of the enhanced MRI signal. The present work expands the possibilities for the design of novel contrast agents, which has to date focused on the modification of the magnetic nanoparticles themselves, by also benefiting from the formation of hybrid materials where the employed carrier might play a key role in the resulting properties.

4. Experimental Section

Materials: Chemical vapor deposition multiwalled carbon nanotubes (MWNTs) were supplied as a dry powder (Thomas Swan & Co. Ltd, UK) with an external average diameter of 10–12 nm (information provided by the supplier). Iron acetate (III), propidium iodide, human male AB plasma, Triton X-100, ribonuclease A, agar, agarose, nitric acid, citric acid, sodium phosphate dibasic (Na_2HPO_4), Pluronic F-127, 10% neutral buffered formalin, paraformaldehyde (PFA), DPX mounting medium, nuclear red solution, and Accustain kit were purchased from Sigma-Aldrich. Xylene and ethanol were purchased from Fisher Scientific (UK). Dulbecco's Modified Eagle Medium (DMEM), PBS, penicillin-streptomycin, Glutamax, and sodium pyruvate were obtained from Invitrogen, Life Sciences (UK). Plasma derived bovine serum (FBS) was obtained from First-Link, UK Ltd. Cytotox 96 Non-Radio Cytotoxicity Assay was bought from Promega UK Ltd. Endorem was obtained from Guerbet (UK). Dipicolylamine-alendronate (DPA-ale or BP) and ^{99m}Tc -BP were synthesized as previously reported.[16] Na[$^{99m}TcO_4$] in physiological saline was obtained from a ^{99}Mo/^{99m}Tc generator

at the Radiopharmacy of Saint Bartholomew's Hospital and The London School of Medicine & Dentistry Queen Mary University, London, UK. Radioactivity in samples was measured using a CRC-15R dose calibrator (Capintec, USA). $[^{99m}Tc\ (CO)_3\ (H_2O)_3]^+$ was synthesized using Isolink kits prepared by Mallinckrodt Medical B.V. (USA). Isoflurane (IsoFlo) for anesthesia was purchased from Abbott Laboratory Ltd (UK).

Preparation of S-SPION-MWNT and L-SPION-MWNT: The as-received MWNTs were purified by steam treatment followed by an HCl wash, as previously described.[26] Briefly, MWNTs were ground with an agate mortar and pestle until a fine powder was obtained and introduced inside a horizontal tubular furnace. Steam was introduced by bubbling argon through hot distilled water. To prepare long MWNTs the sample was exposed to steam at 900 °C for 1.5 h, whereas short MWNTs were achieved after 15 h of steam treatment.[13] The solid powder was next treated with HCl to remove catalytic nanoparticles and washed with water until the pH of the filtrate was neutral. Both S-MWNT and L-MWNT were independently treated with 3 M HNO_3 for 45 h under refluxing conditions. This resulted in the introduction of oxygen bearing functionalities onto the CNT structure, mainly carboxylic acid groups (–COOH). The *f*-MWNTs were collected by filtration and thoroughly washed with distilled water until neutral pH was achieved. The MWNTs were decorated with SPION by in situ formation of the nanoparticles following a previously reported protocol that employs iron (II) acetate as a precursor.[25]

Analysis and Characterization of SPION–MWNTs: TGA was performed on a Netzsch instrument, model STA 449 F1 Jupiter. Experiments were conducted under a flow of air at a heating rate of 10 °C min^{-1} up to 950 °C.

Low magnification TEM images were obtained using a JEOL 1210 and operating at 120 kV. To determine the length distribution of the steam and nitric acid treated MWNTs, a small amount of L-MWNT and S-MWNT was dispersed in absolute ethanol and sonicated for 30 min in an ultrasonic power bath. Afterward, the dispersion was drop dried onto a holey carbon TEM grid covered with an ultrathin C film. The samples of L-SPION-MWNT and S-SPION-MWNT were prepared by dispersing a small amount of sample in 1% Pluronic F-127 (dispersing agent employed in the MRI studies). Afterward, the dispersion was also drop dried onto a holey carbon TEM grid covered with an ultrathin C film.

X-ray diffraction studies were conducted using a powder diffractometer (CuKα_1, λ = 0.1540 nm; Siemens D5000, Germany) with 2θ ranging from 5° to 65°. The PDF (powder data file) database was used to identify the compounds.

X-ray photoelectron spectra were acquired with a Kratos AXIS ultra DLD spectrometer with an Al Kα X-ray font and a power of 120 W. Samples were measured as dry powder. Survey-scan was conducted with a pass energy of 160 eV and high resolution scans at a pass energy of 20 eV. Hybrid-slot lens mode was employed, with an area of analysis of 700 × 300 µm.

Magnetic measurements were done in a SQUID magnetometer (QuantumDesign). A diamagnetic gelatin capsule was filled with 3–4 mg of sample. Data were acquired with an applied field from –50 000 Oe to +50 000 Oe at 10 and 300 K to obtain the hysteresis loops. The sample holder contribution was subtracted in all the measurements, by subtracting the linear high-field magnetization data.

MWNT-SPION Phantom Preparation: S-MWNT-SPION and L-MWNT-SPION in 1% Pluronic F-127 solution were dispersed for 30 min using a bath sonicator (UT-300H) purchased from VWR (UK). Dispersed MWNT-SPION were mixed with an equal volume of melted agar solution (2%, w/v in water) to achieve final phantom concentrations ranging from 0.25×10^{-3} M to 1.25×10^{-3} M (Fe) in 1% agar in water.

MR Imaging of Phantoms: Phantoms were imaged using a 7 Tesla horizontal MR scanner obtained from Varian Inc. (USA). The gradient coil has an inner diameter of 12 cm, gradient strength was 1000 mT m^{-1} (100 G cm^{-1}), and rise-time was 120 µs. Quadrature transmit/receive coil (RAPID) with an internal diameter of 39 mm was obtained from Biomedical GmbH (Germany). Cine-FLASH MRI technique with variable echo time (TE) was used to acquire T_2* images. Cine-FLASH parameters for T_2* images were: FOV (field of view) = 30 × 30 mm, matrix size = 96 × 96, slice thickness = 1 mm; number of slice = 1; flip angle = 20°, 1 average, TR = 700 ms; TE = 1, 2, 3, 5, 8, 10 ms; scan time ≈7 min.

Phantom MR Imaging Analysis: MR images were analyzed using ImageJ (USA). T_2* pixel by pixel data was fitted by the following equation: $S_n = S_0 \times \exp(-TE_n/T_2^*)$. Where S_n is the signal measured, S_0 is the initial signal, and TE_n is the echo spacing. Regions of interest (ROI) in the phantom were selected, three T_2* maps were averaged to provide the mean corresponded T_2* values of such area. R_2* values (corresponding to $1/T_2$*) were calculated and consequently related to the iron concentrations.

Cell Culture and Treatment: J774A.1 cell line (ATCC TIB-67) was cultured in DMEM media supplemented with 10% FBS, 50 U mL^{-1} penicillin, 50 µg mL^{-1} streptomycin, and 1% L-glutamax, at 37 °C in 5% CO_2. Cells were routinely grown in 75 cm^2 canted-neck tissue culture flasks and passaged twice a week by scraping cells at 80% confluency. S-SPION-MWNT and L-SPION-MWNT were dispersed for 30 min in a bath sonicator before use. J774A.1 cells were incubated with SPION-MWNT or Endorem for 24 h, at 12 and 24 µg mL^{-1} of Fe, in J774A.1 cells at 37 °C and 5% CO_2.

Perls' Prussian Blue Staining of J77A.1 Cells: To detect the presence of iron in cells, the Accustain kit from Sigma-Aldrich (UK) was used with minor modifications to the manufacturer's instructions. Treated cells on coverslip were fixed in 4% PFA, washed in PBS, and stained with potassium ferrocyanide solution/HCl solution mixed at 1:1 ratio (v/v) for 20 min to reveal the presence of iron by blue staining. Then, cells were washed in PBS and counterstained after incubation with the Nuclear Red Solution for 10 min. Coverslips were then dehydrated by sequential incubation for 1 min in solutions of ethanol (50%, 70%, 100%) and xylene (two incubations) before being mounted in DPX mounting media. All stained sections were analyzed using a DM 1000 LED Microscope from Leica Microsystems (UK) coupled with CCD camera purchased from Qimaging (UK).

In Vitro Phantom Preparation and Imaging: After treatment, J774A.1 cells were scraped, washed in PBS, and fixed in 4% PFA. Cells were counted and resuspended in 1% agarose solution to achieve a final density of 1×10^6 cells per 200 µL of 0.5% agarose. Phantoms containing J774.A.1 cells were imaged by MRI and analyzed using ImageJ following the same method described above for SPION-MWNT phantoms.

In Vitro Uptake Study Using ICP-MS Detection: The intracellular amount of iron was quantified by ICP-MS to compare the in vitro uptake ability of SPION-MWNT hybrids. J774.A.1 cells were digested in HNO_3 (10:1) at 65 °C overnight. ICP-MS was carried out on Sciex Elan 6100DRC with AS93+ autosampler and crossflow

nebulizer obtained from Perkin Elmer Ltd (UK). Results were analyzed using Elan v3.3 software provided by Perkin Elmer Lts (UK). ^{56}Fe was measured in samples using sample flow of 0.4 ml min^{-1}, nebulizer gas flow of 0.98 L min^{-1}, plasma gas flow of 15 L min^{-1}, aux gas flow 0.8 L min^{-1}, RF power 1200 W, and cell gas NH_3 at 0.7 mL min^{-1}. Triplicates were averaged for each sample, each replicate being 30 sweeps with 100 ms dwell time.

Animals: All in vivo experiments were carried out under the authority of project and personal licenses granted by the UK Home Office and the UKCCCR Guidelines (1998). All in vivo studies were conducted using female C57BL/6 mice (6–8 weeks old) supplied from Harlan Laboratories (UK).

In Vivo MR Imaging: In vivo MR imaging was performed using a 7 Tesla horizontal MR scanner used for phantom MR imaging. Animals were injected with 1.4 or 2.9 mg (Fe) per kg of SPION-MWNT or Endorem followed by imaging after 30 min, 24 h, and 8 d in prone position under anesthesia maintained with 1.5% isoflurane/98.5% oxygen. The body temperature was maintained at 37 °C using a warm air fan. Cine-FLASH MRI technique with variable echo time (TE) was used to acquire T_2* images for in vivo studies. ECG was monitored via two metallic needles placed subcutaneously in the front paws. A pressure-transducer for respiratory gating was placed on the animal abdomen. To synchronize data acquisition with the ECG and to compensate for respiratory motion, simultaneous ECG triggering and respiration gating were applied. Cine-FLASH parameters for T_2* images were: FOV = 25 × 25 mm, matrix size = 128 × 128, slice thickness = 1 mm; flip angle = 20°; number of slice = 1; 1 average; TR = 1/heart rate = RR-interval; TE = 1, 2, 3, 5 ms; scan time ≈5 min.

In Vivo MR Imaging Analysis: MR images were analyzed using ImageJ as described above for phantom MR imaging analysis. ROI in the liver and spleen were selected, five T_2* maps were averaged to provide the mean corresponded T_2* values of such area. R_2* values (corresponding to 1/T_2*) were calculated and related to the acquisition time points.

Radio-Labeling and In Vitro Stability of S-SPION-MWNT: The labeling of S-SPION-MWNT with ^{99m}Tc-BP was carried out as previously reported.[25] A dispersion of S-SPION-MWNT (1 mg mL^{-1}) was obtained by sonication for 10 min in 1% Pluronic F-127/0.9% NaCl solution concentration (w/v) and mixed with ^{99m}Tc-BP (200–500 MBq in 50 µg of BP/125 µL). The mixture was incubated at 37 °C for 30 min with gentle shaking. After cooling to room temperature, ^{99m}Tc-BP-S-MWNT hybrids were separated from unbound ^{99m}Tc-BP by centrifugation at 14 000 rcf for 20 min and the pellets containing ^{99m}Tc-BP-S-MWNT hybrids were washed five times (1 mL each wash) with distilled water until less than 1% of the radioactivity was detected in the supernatant. The pellet was then re-dispersed using 1% Pluronic F-127 solution to achieve a final concentration of 1 mg mL^{-1} for subsequent in vivo studies (γ-scintigraphy and SPECT/CT imaging).

Serum-Stability of the Radio-Labeled Hybrids: The in vitro stability of short hybrids was confirmed by mixing ^{99m}Tc-BP-S-MWNT with an equal volume of human serum or PBS (at 50% final concentration) and incubating samples at 37 °C for 24 h. After sample centrifugation at 14 000 rcf for 20 min, γ-counting was used to measure the radioactivity of the pellets and the supernatants. The percentage of ^{99m}Tc-BP remaining bound to S-SPION-MWNT was above 80% in PBS and 85% in serum, indicating the good stability of short hybrids in PBS and human serum.

Whole Body 3D SPECT/CT Imaging of Mice Injected with 99mTc-BP-S-MWNT: To assess the biodistribution of ^{99m}Tc-BP-S-MWNT in C57BL/6 mice, 10 mg kg^{-1} (≈200 µg per mouse) of ^{99m}Tc-BP-S-MWNT or ^{99m}Tc-BP in 1% Pluronic F-127/0.9% NaCl containing 5–10 MBq was injected intravenously via tail vein. SPECT imaging was carried out immediately after injection with images taken in 16 projections over 30 min using a four-head scanner Nano-SPECT/CT scanner provided by Bioscan (USA) with 1.4 mm pinhole collimators. CT scanning was performed with a 45 kV X-ray source and 1000 ms exposure time over 10 min at the end of each SPECT acquisition. SPECT and CT images were reconstructed using the MEDISO software supplied by Medical Imaging Systems (Hungary) and then merged by the InVivoScope software obtained from Bioscan (USA). Each animal was recovered and further imaged at 4 and 24 h.

Organ Biodistribution of 99mTc-BP-S-MWNT in Mice by γ-Scintigraphy: The pharmacokinetic profile of ^{99m}Tc-BP-S-MWNT was measured by γ-scintigraphy after intravenous injection of ^{99m}Tc-BP-SPION-MWNT dispersed in 1% Pluronic F-127/0.9% NaCl via tail vein. The blood clearance profile was obtained by collecting blood samples in heparinized capillaries from 2 min up to 24 h after injection. In order to study the organ biodistribution, major organs including the skin, liver, spleen, heart, lung, muscle, bone, brain, stomach, and intestine were excised postmortem at 1, 4, and 24 h after injection. Injected mice were kept in metabolic cages for 24 h after injection to collect urine and faeces. Samples were weighed and the radioactivity was detected, quantified, and corrected for physical radioisotope decay by γ-scintigraphy. The % ID per gram tissue was calculated and plotted as the mean of triplicate samples ± SD.

Statistical Analysis: The quantitative in vitro and in vivo data were statistically analyzed by one-way ANOVA with post hoc analysis using the Tukey test and presented as mean ± SD. The quantitative data were also analyzed by one-way ANOVA (*$p < 0.05$, **$p < 0.01$, ***$p < 0.001$).

Supporting Information

Supporting Information is available from the Wiley Online Library or from the author.

Acknowledgements

L.C. and M.B. contributed equally to this work. The authors are grateful to Thomas Swan Co. & Ltd for supplying the Elicarb MWNT samples. L.C. acknowledges a CSIC JAE Predoc Fellowship. M.B. is a Marie Curie Fellow. Funding from FP7-ITN Marie-Curie Network programme RADDEL (290023), Biotechnology and Biological Sciences Research Council (BB/J008656/1), Worldwide Cancer Research (12-1054), and Spanish Ministry of Economy and Competitiveness (MAT2014-53500-R and MAT2014-56063-C2-1R) is acknowledged. R.T.M.D. acknowledges funding by The Centre of Excellence in Medical Engineering funded by the Wellcome Trust and EPSRC under Grant No. WT 088641/Z/09/Z. L.C., J.F., and G.T./ICMAB acknowledge financial support from the Spanish Ministry

of Economy and Competitiveness, through the "Severo Ochoa" Programme for Centres of Excellence in R&D (SEV-2015-0496). K.T.A., G.T, and R.T.M.D. thank the members of the EU COST actions TD1004 (Theranostics Imaging and Therapy: An Action to Develop Novel Nanosized Systems for Imaging-Guided Drug Delivery) and TD1007 (Bimodal PET-MRI molecular imaging technologies and applications for in vivo monitoring of disease and biological processes) for useful discussions. The XPS data were acquired at the Laboratorio de Microscopías Avanzadas (LMA) – Instituto de Nanociencia de Aragón (INA) (Spain).

[1] E. Heister, E. W. Brunner, G. R. Dieckmann, I. Jurewicz, A. B. Dalton, *ACS Appl. Mater. Interfaces* **2013**, *5*, 1870.
[2] Z. Liu, S. Tabakman, K. Welsher, H. Dai, *Nano Res.* **2009**, *2*, 85.
[3] K. Pulskamp, S. Diabaté, H. F. Krug, *Toxicol. Lett.* **2007**, *168*, 58.
[4] a) C. A. Poland, R. Duffin, I. Kinloch, A. Maynard, W. A. H. Wallace, A. Seaton, V. Stone, S. Brown, W. MacNee, K. Donaldson, *Nat. Nano* **2008**, *3*, 423; b) J. Palomäki, E. Välimäki, J. Sund, M. Vippola, P. A. Clausen, K. A. Jensen, K. Savolainen, S. Matikainen, H. Alenius, *ACS Nano* **2011**, *5*, 6861; c) K. Kostarelos, *Nat. Biotechnol.* **2008**, *26*, 774.
[5] A. Shvedova, V. Castranova, E. Kisin, D. Schwegler-Berry, A. Murray, V. Gandelsman, A. Maynard, P. Baron, *J. Toxicol. Environ. Health, Part A* **2003**, *66*, 1909.
[6] C. Bussy, M. Pinault, J. Cambedouzou, M. J. Landry, P. Jegou, M. Mayne-L'hermite, P. Launois, J. Boczkowski, S. Lanone, *Part. Fibre Toxicol.* **2012**, *9*, 46.
[7] S. Hirano, S. Kanno, A. Furuyama, *Toxicol. Appl. Pharmacol.* **2008**, *232*, 244.
[8] a) H. Ali-Boucetta, A. Nunes, R. Sainz, M. A. Herrero, B. Tian, M. Prato, A. Bianco, K. Kostarelos, *Angew. Chem. Int. Ed.* **2013**, *52*, 2274; b) B. Sitharaman, X. Shi, X. F. Walboomers, H. Liao, V. Cuijpers, L. J. Wilson, A. G. Mikos, J. A. Jansen, *Bone* **2008**, *43*, 362; c) K. Kostarelos, *Nat. Biotechnol.* **2008**, *26*, 774; d) A. Bianco, K. Kostarelos, M. Prato, *Chem. Commun.* **2011**, *47*, 10182.
[9] a) L. Lacerda, M. A. Herrero, K. Venner, A. Bianco, M. Prato, K. Kostarelos, *Small* **2008**, *4*, 1130; b) J. Kolosnjaj-Tabi, K. B. Hartman, S. Boudjemaa, J. S. Ananta, G. Morgant, H. Szwarc, L. J. Wilson, F. Moussa, *ACS Nano* **2010**, *4*, 1481; c) L. Lacerda, H. Ali-Boucettal, M. A. Herrero, G. Pastorin, A. Bianco, M. Prato, K. Kostarelos, *Nanomedicine* **2008**, *3*, 149.
[10] a) J. Liu, A. G. Rinzler, H. Dai, J. H. Hafner, R. K. Bradley, P. J. Boul, A. Lu, T. Iverson, K. Shelimov, C. B. Huffman, F. Rodriguez-Macias, Y.-S. Shon, T. R. Lee, D. T. Colbert, R. E. Smalley, *Science* **1998**, *280*, 1253; b) C.-C. Lin, B. T. T. Chu, G. Tobias, S. Sahakalkan, S. Roth, M. L. H. Green, S.-Y. Chen, *Nanotechnology* **2009**, *20*, 105703.
[11] Z. Gu, H. Peng, R. H. Hauge, R. E. Smalley, J. L. Margrave, *Nano Lett.* **2002**, *2*, 1009.
[12] G. Tobias, L. Shao, C. G. Salzmann, Y. Huh, M. L. H. Green, *J. Phys. Chem. B* **2006**, *110*, 22318.
[13] L. Cabana, X. Ke, D. Kepic, J. Oro-Solé, E. Tobías-Rossell, G. Van Tendeloo, G. Tobias, *Carbon*, **2015**, *93*, 1059.
[14] D. Eder, *Chem. Rev.* **2010**, *110*, 1348.
[15] a) S. Datta, L. Marty, J. P. Cleuziou, C. Tilmaciu, B. Soula, E. Flahaut, W. Wernsdorfer, *Phys. Rev. Lett.* **2011**, *107*, 186804; b) J. H. Spencer, J. M. Nesbitt, H. Trewhitt, R. J. Kashtiban, G. Bell, V. G. Ivanov, E. Faulques, J. Sloan, D. C. Smith, *ACS Nano* **2014**, *8*, 9044; c) L. Cabana, B. Ballesteros, E. Batista, C. Magén, R. Arenal, J. Oró-Solé, R. Rurali, G. Tobias, *Adv. Mater.* **2014**, *26*, 2016; d) D. Golberg, P. M. F. J. Costa, M.-S. Wang, X. Wei, D.-M. Tang, Z. Xu, Y. Huang, U. K. Gautam, B. Liu, H. Zeng, N. Kawamoto, C. Zhi, M. Mitome, Y. Bando, *Adv. Mater.* **2012**, *24*, 177.
[16] a) S. Hong, G. Tobias, K. Al Jamal, B. Ballesteros, H. Ali Boucetta, S. Lozano Perez, P. Nellist, R. Sim, C. Finucane, S. Mather, M. L. H. Green, K. Kostarelos, B. Davis, *Nat. Mater.* **2010**, *9*, 485; b) M. Martincic, G. Tobias, *Expert Opin. Drug Delivery* **2015**, *12*, 563; c) X. Liu, I. Marangon, G. Melinte, C. Wilhelm, C. Ménard-Moyon, B. P. Pichon, O. Ersen, K. Aubertin, W. Baaziz, C. Pham-Huu, S. Bégin-Colin, A. Bianco, F. Gazeau, D. Bégin, *ACS Nano* **2014**, *8*, 11290; d) J. J. Law, A. Guven, L. J. Wilson, *Contrast Media Mol. Imaging* **2014**, *9*, 409; e) Y. Liu, B. W. Muir, L. J. Waddington, T. M. Hinton, B. A. Moffat, X. Hao, J. Qiu, T. C. Hughes, *Biomacromolecules* **2015**, *16*, 790.
[17] a) G. Lamanna, A. Garofalo, G. Popa, C. Wilhelm, S. Begin-Colin, D. Felder-Flesch, A. Bianco, F. Gazeau, C. Menard-Moyon, *Nanoscale* **2013**, *5*, 4412; b) J. T.-W. Wang, C. Fabbro, E. Venturelli, C. Ménard-Moyon, O. Chaloin, T. Da Ros, L. Methven, A. Nunes, J. K. Sosabowski, S. J. Mather, M. K. Robinson, J. Amadou, M. Prato, A. Bianco, K. Kostarelos, K. T. Al-Jamal, *Biomaterials* **2014**, *35*, 9517; c) Z. Liu, W. Cai, L. He, N. Nakayama, K. Chen, X. Sun, X. Chen, H. Dai, *Nat. Nano* **2007**, *2*, 47.
[18] M. R. McDevitt, D. Chattopadhyay, B. J. Kappel, J. S. Jaggi, S. R. Schiffman, C. Antczak, J. T. Njardarson, R. Brentjens, D. A. Scheinberg, *J. Nucl. Med.* **2007**, *48*, 1180.
[19] P. A. Rinck, *Magnetic Resonance in Medicine. The Basic Textbook of the European Magnetic Resonance Forum*, 8th ed., Blackwell Science, Berlin, Germany **2014**, (electronic version 8.2).
[20] L. A. Tran, M. Hernández-Rivera, A. N. Berlin, Y. Zheng, L. Sampaio, C. Bové, M. d. G. Cabreira-Hansen, J. T. Willerson, E. C. Perin, L. J. Wilson, *Biomaterials* **2014**, *35*, 720.
[21] J. H. Choi, F. T. Nguyen, P. W. Barone, D. A. Heller, A. E. Moll, D. Patel, S. A. Boppart, M. S. Strano, *Nano Lett.* **2007**, *7*, 861.
[22] M. Yin, M. Wang, F. Miao, Y. Ji, Z. Tian, H. Shen, N. Jia, *Carbon* **2012**, *50*, 2162.
[23] H. Wu, G. Liu, Y. Zhuang, D. Wu, H. Zhang, H. Yang, H. Hu, S. Yang, *Biomaterials* **2011**, *32*, 4867.
[24] Y. Liu, T. C. Hughes, B. W. Muir, L. J. Waddington, T. R. Gengenbach, C. D. Easton, T. M. Hinton, B. A. Moffat, X. Hao, J. Qiu, *Biomaterials* **2014**, *35*, 378.
[25] J. T. W. Wang, L. Cabana, M. Bourgognon, H. Kafa, A. Protti, K. Venner, A. M. Shah, J. K. Sosabowski, S. J. Mather, A. Roig, X. X. Ke, G. Van Tendeloo, R. T. M. Rosales, G. Tobias, K. T. Al-Jamal, *Adv. Funct. Mater.* **2014**, *24*, 1880.
[26] B. Ballesteros, G. Tobias, L. Shao, E. Pellicer, J. Nogués, E. Mendoza, M. L. H. Green, *Small* **2008**, *4*, 1501.
[27] L. Shao, G. Tobias, C. G. Salzmann, B. Ballesteros, S. Y. Hong, A. Crossley, B. G. Davis, M. L. H. Green, *Chem. Commun.* **2007**, 5090.
[28] P. Raffa, D. A. Z. Wever, F. Picchioni, A. A. Broekhuis, *Chem. Rev.* **2015**, *115*, 8504.
[29] A. P. Grosvenor, B. A. Kobe, M. C. Biesinger, N. S. McIntyre, *Surf. Interface Anal.* **2004**, *36*, 1564.
[30] J. S. Ananta, M. L. Matson, A. M. Tang, T. Mandal, S. Lin, K. Wong, S. T. Wong, L. J. Wilson, *J. Phys. Chem. C* **2009**, *113*, 19369.
[31] D. Serantes, D. Baldomir, M. Pereiro, C. E. Hoppe, F. Rivadulla, J. Rivas, *Phys. Rev. B* **2010**, *82*, 134433.
[32] S. Si, A. Kotal, T. Mandal, S. Giri, H. Nakamura, T. Kohara, *Chem. Mater.* **2004**, *16*, 3489.
[33] a) S. Laurent, D. Forge, M. Port, A. Roch, C. Robic, L. Vander Elst, R. N. Muller, *Chem. Rev.* **2008**, *108*, 2064; b) R. A. Brooks, *Magn. Reson. Med.* **2002**, *47*, 388.
[34] P. Gillis, F. Moiny, R. A. Brooks, *Magn. Reson. Med.* **2002**, *47*, 257.
[35] a) Y. Matsumoto, A. Jasanoff, *Magn. Reson. Imaging* **2008**, *26*, 994; b) D. X. Chen, E. Taboada, A. Roig, *J. Magn. Magn. Mater.* **2011**, *323*, 2487.

[36] a) S. Laus, B. Sitharaman, É. Tóth, R. D. Bolskar, L. Helm, S. Asokan, M. S. Wong, L. J. Wilson, A. E. Merbach, *J. Am. Chem. Soc.* **2005**, *127*, 9368; b) S. Laus, B. Sitharaman, É. Tóth, R. D. Bolskar, L. Helm, L. J. Wilson, A. E. Merbach, *J. Phys. Chem. C* **2007**, *111*, 5633; c) R. Bolskar, in *Medicinal Chemistry and Pharmacological Potential of Fullerenes and Carbon Nanotubes*, Vol. *1* (Eds: F. Cataldo, T. Da Ros), Springer,Netherlands **2008**, p. 157.

[37] G. Bardi, A. Nunes, L. Gherardini, K. Bates, K. T. Al-Jamal, C. Gaillard, M. Prato, A. Bianco, T. Pizzorusso, K. Kostarelos, *PLoS ONE* **2013**, *8*, e80964.

[38] R. Torres Martin de Rosales, C. Finucane, S. J. Mather, P. J. Blower, *Chem. Commun.* **2009**, 4847.

Received: September 8, 2015
Revised: March 9, 2016
Published online: April 15, 2016

